



# Formation of vortices on a tubercled wing, and their effects on drag



Michael D.P. Bolzon\*, Richard M. Kelso, Maziar Arjomandi

The University of Adelaide, Adelaide, 5005, Australia

## ARTICLE INFO

### Article history:

Received 7 December 2015

Received in revised form 24 June 2016

Accepted 30 June 2016

Available online 9 July 2016

## ABSTRACT

Wake surveys of 2 swept NACA 0021 wings were conducted at angles of attack of  $0^\circ$ ,  $3^\circ$ ,  $6^\circ$ ,  $9^\circ$ , and  $12^\circ$ . One wing had a smooth leading edge and the other had a tubercled leading edge. Sweeping the tubercled wing resulted in one vortex in each vortex pair being at least 4 times stronger than the other. There was little difference between the strength of the wingtip vortices of either wing at  $3^\circ$ . From  $6^\circ$  onwards tubercles reduced the strength of the wingtip vortex. The tubercle troughs tended to produce local maxima and minima in the profile and induced drag coefficients, respectively. The converse was true over the peaks. The change in the profile, induced, and total drag coefficients primarily arose from over the wingspan; there was little contribution from the wingtip region.

© 2016 Elsevier Masson SAS. All rights reserved.

## 1. Introduction

Humpback whales are enormous creatures, yet they remain remarkably agile. They can execute underwater somersaults and swim at high angles of attack during feeding [1], feats unique among Baleen whales. Their pectoral flippers are also unique, featuring bumps on the leading edges, termed tubercles, and it is now known that these tubercles are, in part, responsible for the Humpback whale's nimbleness [2].

Tubercles can be categorised by two main parameters, the amplitude, which refers to the distance between a tubercle peak and neighbouring trough, and the wavelength, which refers to the distance between two neighbouring tubercle troughs or peaks. Research has revealed that tubercles create pairs of counter-rotating, streamwise vortices [3–5] as shown in Fig. 1. It was proposed by Hansen et al. [6] that the strength of these vortices is directly related to the Amplitude-to-Wavelength ratio, where increasing this ratio would result in a greater local sweep of the leading edge and an increase in the vortices' strengths. To the authors' knowledge there have been no investigations into the effect of wing sweep on the relative strengths of the pairs of streamwise, counter-rotating vortices.

The main effects of tubercles are a softening and delaying of stall [2,7–9], however, they can also provide significant reductions in drag, as well as increases in the lift-to-drag ratio, for a swept wing at pre-stall angles of attack [10,11]. The aim of the present study is to further investigate the effects of tubercles on swept wing drag, and to determine how tubercles are able to reduce drag.

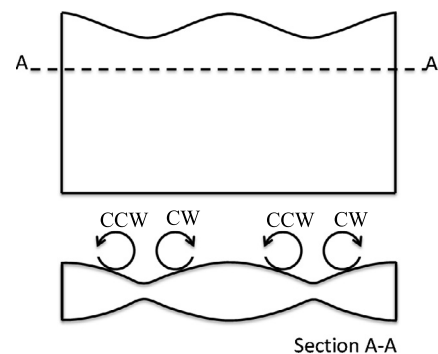


Fig. 1. Diagram of a wing with leading edge tubercles and the approximate location and sign of the vortices produced. CCW refers to a counter-clockwise rotation and CW refers to a clockwise rotation.

To investigate the counter-rotating, streamwise vortex pairs produced by the tubercles, a wake survey has been conducted on the same two wings used in Bolzon et al. [10]. From this wake survey the vorticity distributions and the profile and induced drag coefficients of these wings have been calculated and compared.

## 2. Methodology

### 2.1. Wing configurations

Two NACA 0021 wings, swept at a quarter-chord angle of  $35^\circ$ , were CNC machined from aluminium. One wing had a smooth leading edge, whereas the other wing had tubercles with an amplitude of 10.5 mm and a wavelength of 60 mm along its entire leading edge. The tubercles were machined to preserve a constant

\* Corresponding author.

E-mail address: michael.bolzon@adelaide.edu.au (M.D.P. Bolzon).

## Nomenclature

$\bar{b}$	Normalized span	$U_\infty$	Upstream velocity in $x$ -direction	m/s
$C_{D_I}$	Induced drag coefficient	$u$	Downstream velocity in $x$ -direction	m/s
$C_{D_P}$	Profile drag coefficient	$v$	Downstream velocity in $y$ -direction	m/s
$C_{D_{Total}}$	Total drag coefficient	$w$	Downstream velocity in $z$ -direction	m/s
$D_I$	Induced drag	$\Gamma_{vel}$	Circulation calculated from velocity distribution	$\text{m}^2/\text{s}$
$D_P$	Profile drag	$\Gamma_{vor}$	Circulation calculated from vorticity distribution	$\text{m}^2/\text{s}$
$P_{D_\infty}$	Upstream dynamic pressure	$\rho$	Downstream density of air	$\text{kg}/\text{m}^3$
$P_{S_\infty}$	Upstream static pressure	$\rho_\infty$	Upstream density of air	$\text{kg}/\text{m}^3$
$P_T$	Downstream total pressure	$\sigma$	Cross-flow source	$1/\text{s}$
$P_{T_\infty}$	Upstream total pressure	$\omega$	Vorticity	$\text{s}^{-1}$
$S$	Downstream surface perpendicular to wake, also referred to as “wake plane”			

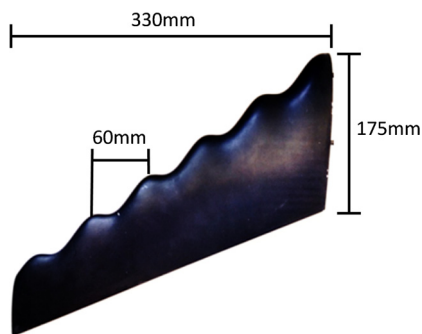


**Fig. 2.** Tubercled wing shown. Tubercles have an amplitude of 10.5 mm and a wavelength of 60 mm. Both wings are the same except for the addition of tubercles.

thickness-to-chord ratio along the wing span, which resulted in a chordwise ridge to form over each tubercle peak and a valley to form in each tubercle trough. These ridges and valleys washed-out towards the trailing-edge. The tubercled wing can be seen in Fig. 2. The amplitude has not been dimensioned as the sweep visually affects the amplitude dimension. Apart from the tubercles, the wings were exactly the same and had the same reference area. The wings had a span of 330 mm, a Mean Aerodynamic Chord, MAC, of 130 mm, and a taper ratio of 0.4. A non-unity taper ratio was chosen as swept wings are typically tapered in an effort to reduce lift production at the wingtip and hence induced drag.

### 2.2. Wake survey

Wake surveys were conducted in the open-jet “KC wind tunnel” at The University of Adelaide. The wind tunnel had a turbulence intensity of 0.6 ~ 0.8% and was operated at a freestream velocity of 27.5 m/s, which resulted in a MAC Reynolds number of 225,000. The experimental setup can be seen in Fig. 3.

The wings were mounted on a JR3 45E15A-163 load cell such that the lift at  $0^\circ$  corresponded solely to the  $z$ -axis direction of the load cell, and the drag to the  $x$ -axis. The wings were then deemed aligned to  $0^\circ$  when the  $z$ -axis load was zero. The misalignment error resulting from the CNC machined wings and the rotary table was estimated to be  $\pm 0.05^\circ$ . The following five angles of attack were surveyed:  $0^\circ$ ,  $3^\circ$ ,  $6^\circ$ ,  $9^\circ$  and  $12^\circ$ . Three runs were conducted for each wing and the averages were then calculated.

A multi-hole pressure probe was located 3 MACs downstream of the wing root trailing edge on a two-directional traverse. This traverse moved the probe to a predefined grid located in the  $y$ - $z$  plane, as shown in Fig. 3, known as a wake plane. The size of this wake plane was dependent on the wing's angle of attack, whereby a higher angle of attack typically resulted in a greater wake size. A greater wake plane size resulted in a longer experimental time,

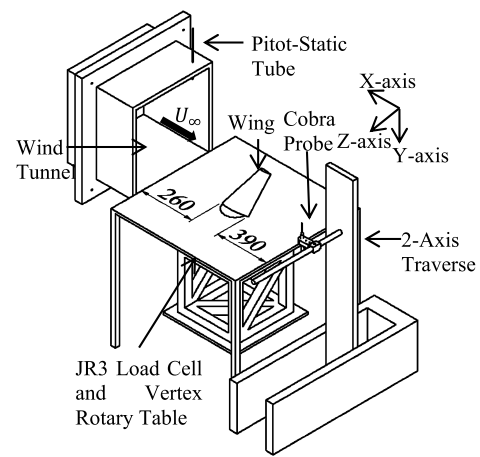


**Fig. 3.** Wake survey experimental setup in open-return wind tunnel. Cobra probe located at 390 mm downstream of the wing trailing edge.

which was not only more impractical, but also resulted in the instruments drifting further from their calibrations, thereby reducing the accuracy of the experiment. To reduce the experimental time the area surveyed was different for each angle of attack, but was kept constant between the two wings. The area surveyed was divided into nodes with a distance of 6 mm between each node. This spacing was chosen as a compromise between experimental time and accuracy.

An off-the-shelf Turbulent Flow Instrumentation brand multi-hole pressure probe, known as a Cobra Probe, was used for these experiments. The Cobra probe had a head size of 3 mm  $\times$  3 mm and a sampling frequency of 600 Hz [12]. This particular multi-hole probe measured 4 pressures from which the three orthogonal downstream velocities,  $u$ ,  $v$ , and  $w$  were calculated from factory calibration curves [12], as found in Shepherd [13]. The measured mean velocity fields were then used to determine the vorticity in the  $y$ - $z$  plane, as shown by Eq. (1). Note that a body-fixed reference frame was used. Any errors in the vorticity calculations arising from the flow quality were accounted for by subtracting the cross-flow velocities of the wake plane without a wing present from the cross-flow velocities with the wings present. A vortex's circulation can be calculated using either Eqs. (2) and (3), however, the circulation calculated from Eq. (2) is typically more accurate than the circulation calculated from Eq. (3) [13]. Therefore, Eq. (2) was used for the remainder of this study to calculate the circulation of any vortex. The region of integration, ROI, was determined in the same manner as in Hassan et al. [14], whereby the maximum vorticity in a given region was found, then each neighbouring point was included in the ROI if its vorticity was within a given threshold and the distance between this point and the point of

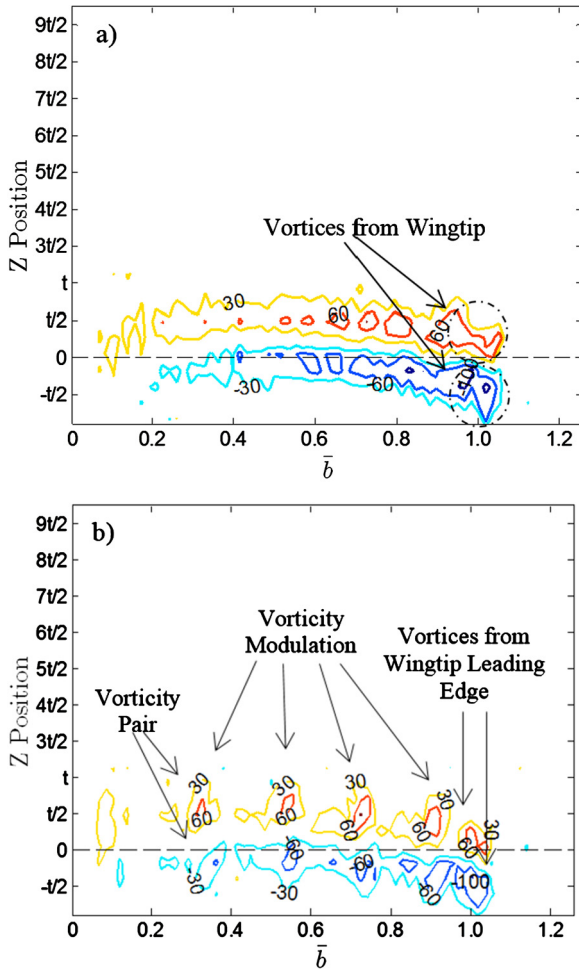


Fig. 4. Vorticity, 1/s, contour of a) smooth, and b) tubercled wings at  $0^\circ$ .

maximum vorticity was within a predefined limit. For all circulations calculated, the vorticity thresholds were  $-30$  1/s and  $30$  1/s for negative and positive vortices, respectively, which from  $3^\circ$  to  $12^\circ$  typically resulted in the demarcation of the tubercle vortices from each other, and from the vortex sheet. When these thresholds did not differentiate a tubercle vortex, a tubercle vortex was defined as from its vortex core to the point of minimum vorticity between this vortex and any other vortex. The vorticity thresholds were sufficient to define the tubercled wing's tip vortex from the vortex sheet. To define the wingtip vortex from neighbouring tubercle vortices, the edge of the wingtip vortex was taken as the point of minimum vorticity between the wingtip vortex and any other vortex. The smooth wing's wingtip vortex was defined from the vortex sheet by implementing the same distance from the wingtip vortex core to the outer edges determined for the tubercled wing's tip vortex. Forward-difference, central-difference, and fourth-order polynomial schemes were considered for the vorticity, and it was found that the forward-difference scheme consistently gave the most accurate induced drags while the fourth-order polynomial consistently gave the least accurate induced drags. Therefore, the forward-difference scheme was used for the calculation of both the vorticity and the source terms.

The induced and profile drags were calculated from wake survey measurements from Eqs. (4) to (10) [15]. Equations (6) and (7) were solved via the Gauss–Siedel iterative method. The equations were deemed solved once the root-mean-square of the difference between sequential iterations was less than  $10^{-7}$ , which resulted in the induced drags of both wings at all tested angles of attack to

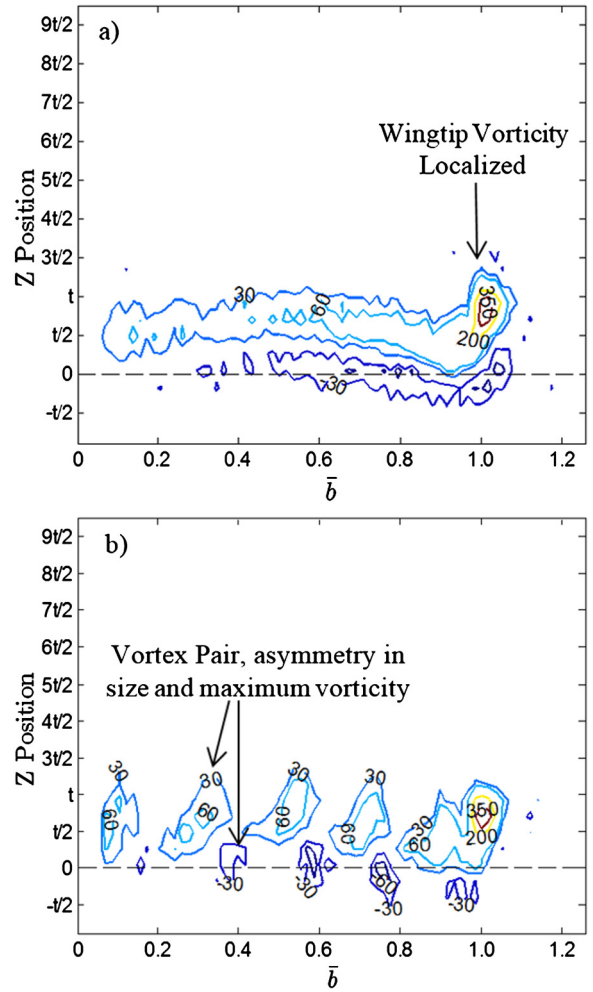


Fig. 5. Vorticity, 1/s, contour of a) smooth, and b) tubercled wings at  $3^\circ$ .

converge. The Dirichlet boundary condition of  $\psi$  is 0 and the Neumann boundary condition of  $\partial\phi/\partial n$  is 0 at the shear layer were used [15]. Typically this method is used for closed-return wind tunnels [15,16]. However, this method can be used in an open-jet wind tunnel if the flow only enters through one plane upstream and leaves through the downstream plane that encompasses the wake plane, as this will approximate a closed-return wind tunnel configuration.

$$\omega = \left( \frac{\partial w}{\partial y} - \frac{\partial v}{\partial z} \right) \quad (1)$$

$$\Gamma_{vel} = \oint_c (v dy + w dz) \quad (2)$$

$$\Gamma_{vor} = \iint_s \omega ds \quad (3)$$

Any errors in the drag calculations that were associated with the flow quality were accounted for by subtracting the induced, profile, and total drag coefficients of the wake plane without either wing present from the induced, profile, and total drag coefficients, respectively, of each wing [14]. The induced, profile, and total drag coefficients of the tubercled wing have been corrected from  $0^\circ$  to  $9^\circ$  to produce coefficients if the tubercled wing were to produce the same lift coefficient as the smooth wing. The  $12^\circ$  angle of attack was not corrected as the extrapolation of data in this region is not accurate due to unknown flow separation. The

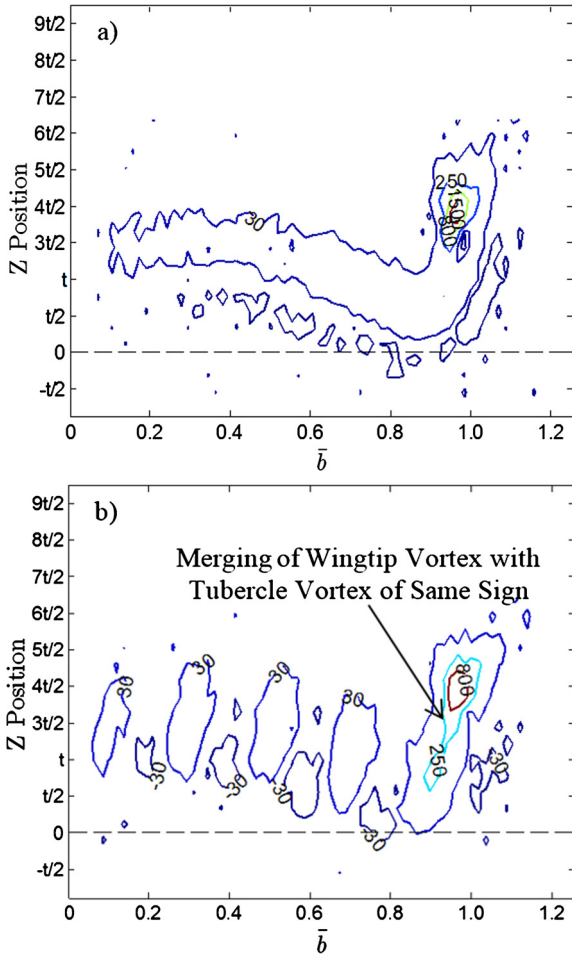


Fig. 6. Vorticity, 1/s, contour of a) smooth, and b) tubercled wings at 9°.

corrections were spline interpolations. Both the uncorrected and corrected values are presented in 3.2. In addition, the same method of correction has been applied to the wingtip vortex strength of the tubercled wing from 3° to 9°, and both the uncorrected and corrected values are presented in 3.1.

As the objects tested were streamline bodies, and there were no obvious defects, only in a high lift configuration would the wing sufficiently redirect flow such that flow would exit the control volume laterally. Preliminary experiments demonstrated that the wake of the wings from 0° to 9° stayed well within the survey area, and evidence can be seen from the vorticity distributions in Figs. 4 to 7. Therefore, for angles of attack within this range, the wake was sufficiently traversed. At an angle of attack of 12° most of the wake was still traversed, however, there were some small sections that were not, as can be seen on the outskirts of the vorticity distribution in Fig. 8. These regions were intentionally excluded from the traversed area to reduce the experimental time and potentially increase the accuracy of the experiments because the instruments would better approximate their initial calibrations. This did not result in an appreciable error in the induced drag calculation.

The variables that are measured for use in Eqs. (4) to (10) are  $P_{T\infty}$ ,  $P_T$ ,  $\rho_\infty$ ,  $\rho$ ,  $u$ ,  $v$ ,  $w$ , and  $U_\infty$ . The  $P_{T\infty}$  was measured by an MKS brand Baratron that was connected to the Pitot port of an upstream Pitot-static probe. A Scanivalve brand DSA3217 pressure scanner was connected to the static port. The  $P_T$  was measured by the Cobra probe. The flow was considered incompressible, therefore, the  $\rho_\infty$  was assumed to be the same as the  $\rho$ . Both of the densities were calculated through the temperature, baromet-

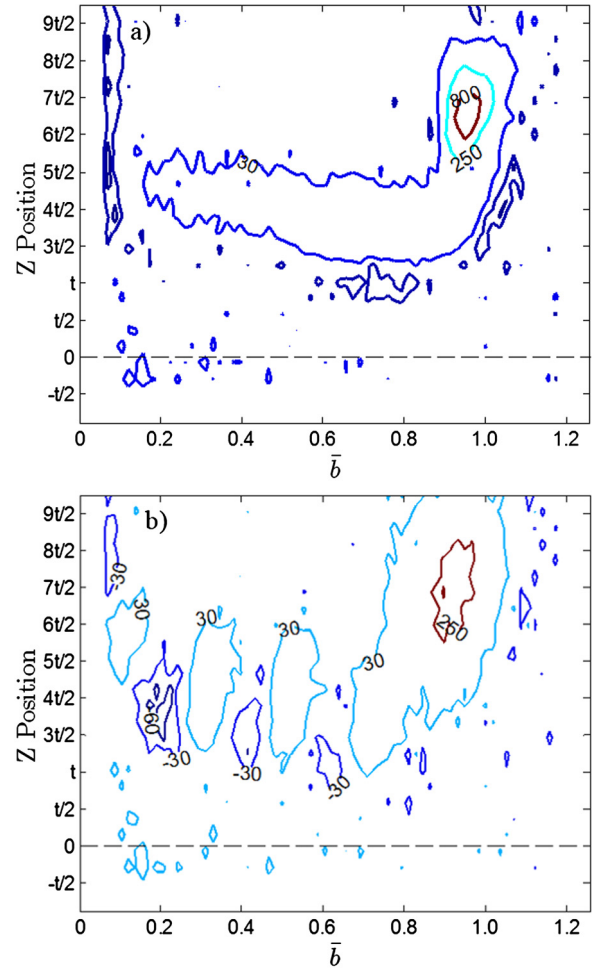


Fig. 7. Vorticity, 1/s, contour of a) smooth, and b) tubercled wings at 12°.

ric pressure, and relative humidity. The temperature was measured from a TSI brand IFA300 constant temperature anemometer module, the barometric pressure was measured from a Bosh brand BMP085 module, and the humidity was measured from a DHT22 module. The BMP085 and DHT22 modules were connected to an Arduino Uno R3, which was connected serially to the data acquisition system. The  $u$ ,  $v$ , and  $w$  velocities were measured by the Cobra probe. The  $U_\infty$  was calculated from the  $P_{D\infty}$ , which was calculated from the difference between the measurements of the Pitot and static ports of the Pitot-static probe, and the density.

$$D_I \approx \frac{1}{2} \rho_\infty \iint_S (\psi \omega - \phi \sigma) dy dz \quad (4)$$

where

$$\sigma = \frac{\partial v}{\partial y} + \frac{\partial w}{\partial z} \quad (5)$$

and

$$\frac{\partial^2 \psi}{\partial y^2} + \frac{\partial^2 \psi}{\partial z^2} = -\omega \quad (6)$$

and

$$\frac{\partial^2 \phi}{\partial y^2} + \frac{\partial^2 \phi}{\partial z^2} = \sigma \quad (7)$$

$$D_P = \iint_S \left[ P_{T\infty} - P_T + \frac{\rho}{2} (U^* - u)(U^* + u - 2U_\infty) \right] dy dz \quad (8)$$

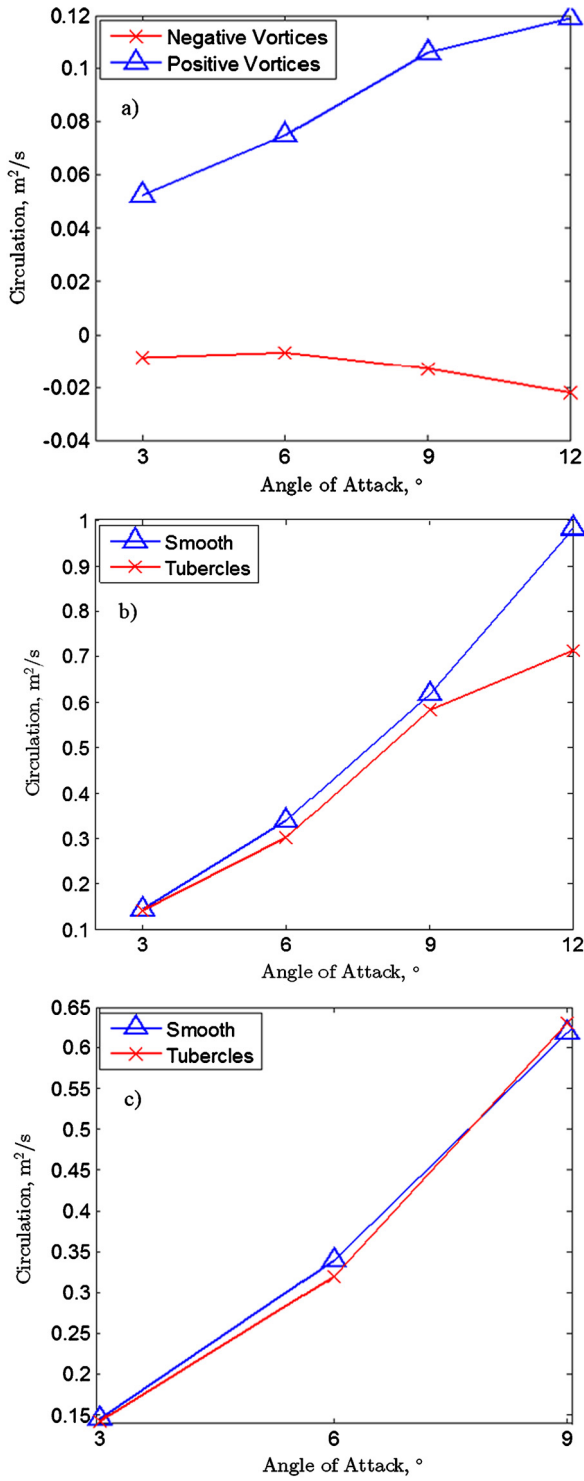


**Fig. 8.** Average circulation of negatively and positively signed vortices of the tubercled wing, a). Wingtip vortex strength of smooth and tubercled wings, b), at 3°, 6°, 9°, and 12°. Corrected wingtip vortex strength of smooth and tubercled wings, c), at 3°, 6°, and 9°.

where

$$U^* = \sqrt{u^2 + \left(\frac{2}{\rho}\right)(P_{T\infty} - P_T)} \quad (9)$$

and

$$u' = U^* - U_\infty \quad (10)$$

**Table 1**

The 95% confidence intervals of the measurements taken during the wake surveys, and the percentage uncertainty of the typical values measured.

Instrument	Variable measured	95% confidence interval (of typical value)
Baratron	$P_{T\infty}, P_{D\infty}$	$\pm 0.5$ Pa ( $\pm 0.1\%$ of $P_{D\infty}$ )
Scanivalve	$P_{S\infty}, P_{D\infty}$	$\pm 3.0$ Pa ( $\pm 0.6\%$ of $P_{D\infty}$ )
Cobra probe	$u$	$\pm 0.45$ m/s ( $\pm 1.75\%$ )
	$v$	$\pm 0.31$ m/s ( $\pm 17\%$ )
	$w$	$\pm 0.31$ m/s ( $\pm 29\%$ )
IFA300	Temperature	$\pm 0.1$ °C ( $\pm 0.03\%$ )
BMP085	Barometric pressure	$\pm 5$ Pa (negligible)
DHT22	Relative humidity	$\pm 2\%$

### 2.3. Uncertainty analysis

The uncertainties in the drag, induced, and profile drag coefficients were calculated via the ‘‘Jitter Method’’ [17–19]. A 95% confidence interval was used for all measurements, and the uncertainties of the instruments for the typical measuring ranges during these experiments are presented in Table 1. Only the Scanivalve and the BMP085 module significantly drifted; 0.12 Pa/hr and 0.01 Pa/hr, respectively. Due to the method used to calculate the induced drag, and subsequently the induced drag coefficient, the uncertainty arising from linear effects of  $v$  and  $w$  velocities on the induced drag was used.

## 3. Results

### 3.1. Vorticity and circulation

Vorticity contours for both wings at 0°, 3°, 9°, and 12° are given in Figs. 4 to 9, 6° is omitted as no new trends appeared. While the wings were mounted vertically, as shown in Fig. 3, it should be noted that the contour maps have been rotated such that the wing span corresponds to the  $x$ -axis of each figure and the  $y$ -axis corresponds to the direction perpendicular to the wing surface. The  $x$ -axes of the contour maps have been normalized to the half-wingspan such that 0 corresponds to the wing root and 1 to the wingtip. The  $y$ -axes have been normalized to the MAC thickness of the wing. The origins of the  $y$ -axes correspond to the projection of the wing chord-line at a given angle of attack. Dashed lines have been included, spanning the entire window along the  $y$ -axes coordinates of 0. Positive vorticity is counter-clockwise rotation. For all angles of attack there are uniform regions of vorticity extending over most of the wingspan, however, tubercles modulate the vorticity into regions of high and lower vorticity, as shown in Fig. 4a) and b). These regions of vorticity are produced by the tubercles [3,4]. The wings were well aligned, as shown by the similarity in the vorticity in the wingtip regions in Fig. 4a) and b). At non-zero angles of attack, the sizes of the vorticity regions produced by a pair of streamwise, counter-rotating vortices are asymmetrical with one vorticity region consistently being larger and having a greater absolute maximum vorticity, as labelled in Fig. 5b). The average circulations of the negatively signed and positively signed vortices for the tubercled wing at 3°, 6°, 9°, and 12° are given in Fig. 8a); for all angles of attack considered, the positively signed vortices are on average 6 times stronger than the negatively signed vortices. Therefore, by sweeping the tubercled wing one vortex in each pair becomes stronger than the other instead of being equal in strength, as is the case for an unswept wing [20]. Increasing the sweep of a wing should logically result in an increased disparity between the strength of the tubercle vortices. Lin [21] suggested that generally, counter-rotating vortices are more effective at controlling two-dimensional flow separation, whereas co-rotating vortices are more effective for three-dimensional flow

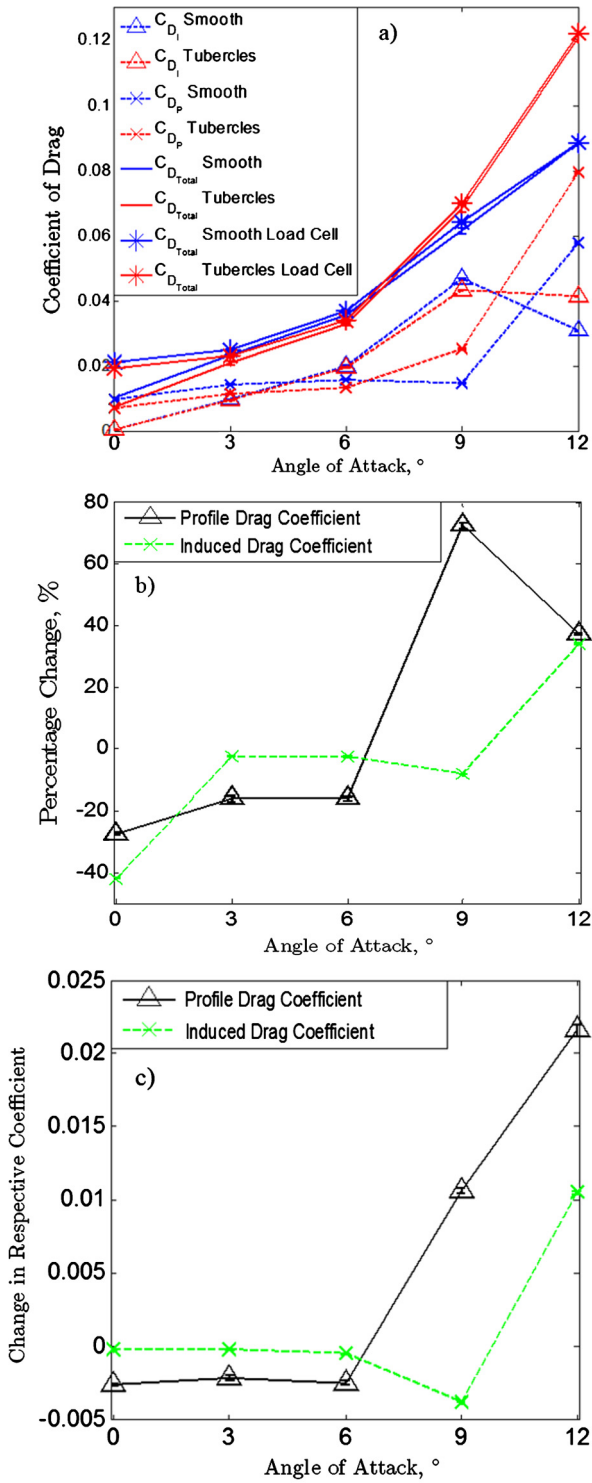


Fig. 9. Total drag and its components breakdown, a), the relative effect of tubercles on the profile and induced drag, b), the absolute effect of tubercles on the profile and induced drag, c). Note: for b) and c), negative means a reduction.

separation, such as on a swept wing. Therefore, as tubercles act like vortex generators [3] this disparity in the vortices' strengths may be beneficial in keeping the flow attached over the swept wing.

As the angle of attack increases the strength of the vortices produced by the tubercles increases, which would result in a greater boundary layer momentum exchange [7], and thereby result in the flow staying attached to a higher angle of attack.

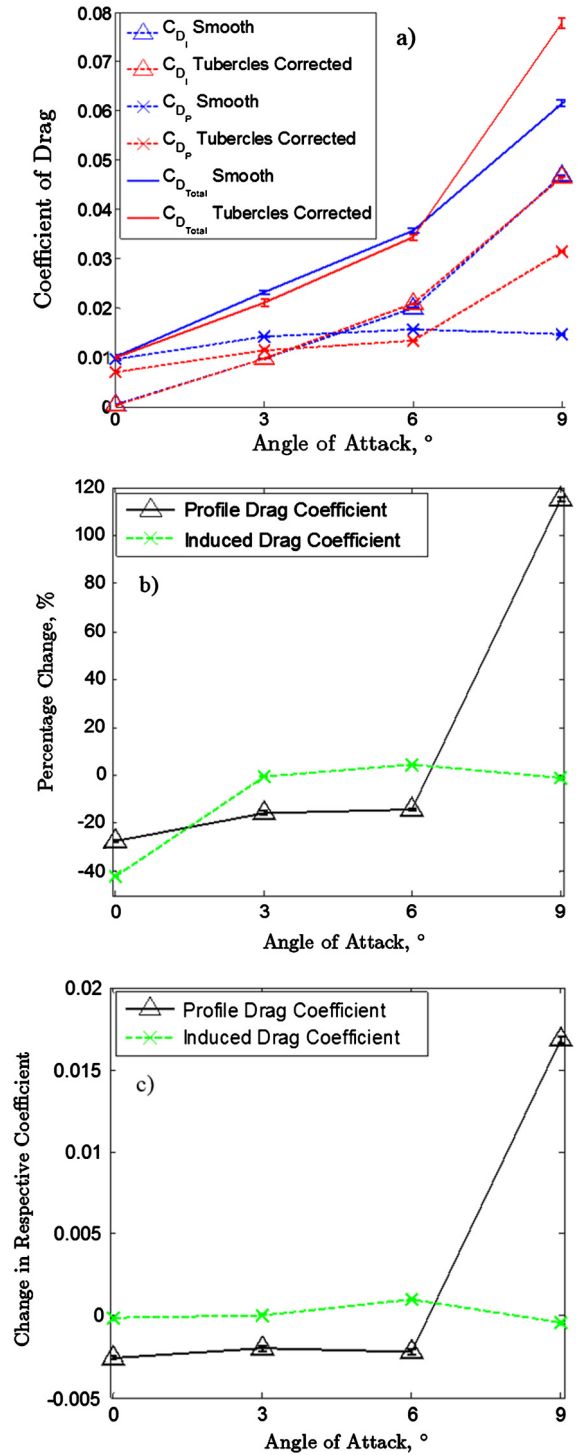


Fig. 10. Corrected total drag and its components breakdown, a), the relative effect of tubercles on the corrected profile and induced drag, b), the absolute effect of tubercles on the corrected profile and induced drag, c). Note: for b) and c), negative means a reduction.

At 3°, 6°, and 9° the vorticity in the wingtip region, ostensibly due to the wingtip vortex is localized to a small area for both the smooth and tubercled wings, as labelled in Fig. 4a) as an example. However, at 12° the wingtip vorticity of the tubercled wing suddenly expands and occupies a much larger region than at the lower angles of attack, which suggests that the flow over the wingtip is largely separating. The uncorrected circulations of the wingtip vortices of both wings at 3°, 6°, 9°, and 12° are given in Fig. 8b); there is little difference in the wingtip strength of either

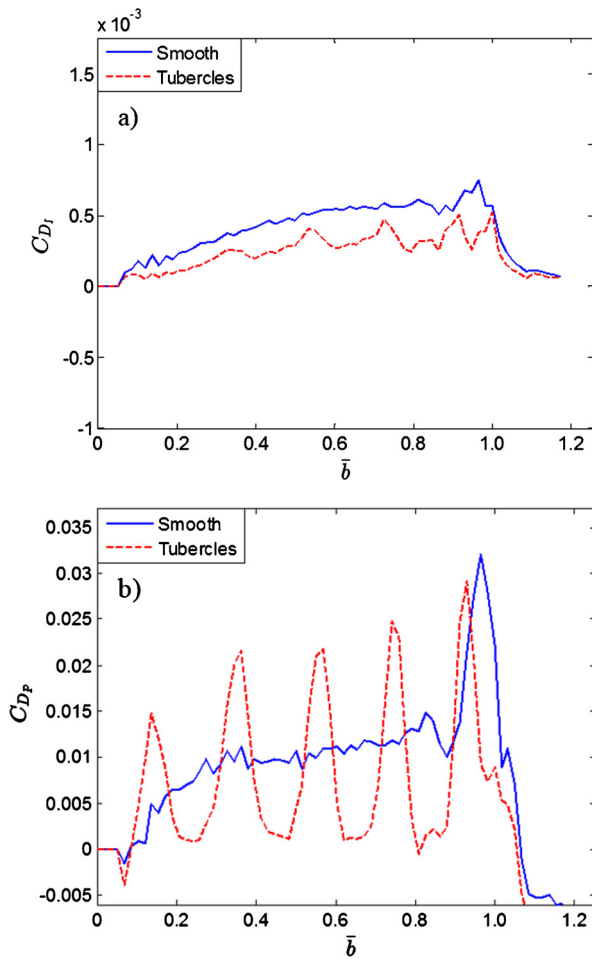


Fig. 11. Spanwise induced, a), and profile, b), drag coefficient distributions for smooth and tubercled wings at  $0^\circ$ .

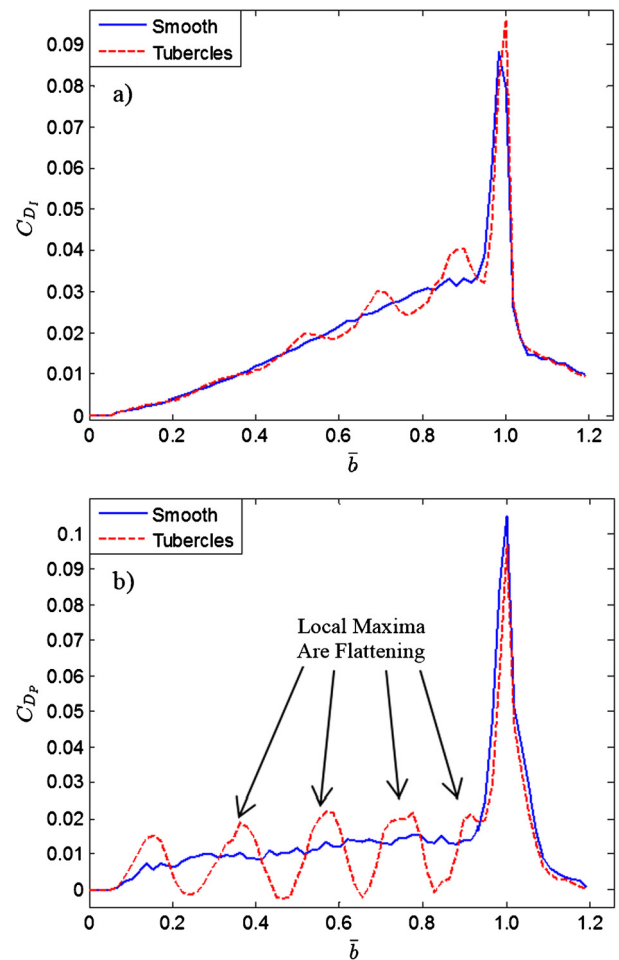


Fig. 12. Spanwise induced, a), and profile, b), drag coefficient distributions for smooth and tubercled wings at  $6^\circ$ .

wing at  $3^\circ$ , however, from  $6^\circ$  to  $9^\circ$  the smooth wingtip vortex is stronger than the tubercled wingtip vortex by approximately 8.5%. At  $12^\circ$ , tubercles reduce the wingtip vortex strength by 27.2%. The reduced wingtip vortex strength may be beneficial for some applications as it may lead to a shorter breakdown length-scale. Fig. 8c) shows that if the tubercled wing were to produce the same lift coefficient as the smooth wing, tubercles would have little effect on the wingtip vortex strength from  $3^\circ$  to  $9^\circ$ .

As expected, for non-zero degree angles of attack the tubercled wing's wingtip vortex tends to merge with tubercle vortices of the same sign, as labelled on Fig. 6b).

### 3.2. Drag breakdown

The total drag coefficients for both wings at all angles of attack considered have been calculated and compared to the force measurements of these exact wings found in Bolzon et al. [9,10]. Note that a full comparison can be found in [9]. Fig. 9a) shows that there is good agreement between the wake survey total drag coefficients and the load cell total drag coefficients for  $3^\circ$  to  $12^\circ$ . Furthermore, the relative effects of tubercles on the total drag coefficients for these angles of attack are within 2%. There is a significant difference between the wake survey and the load cell total drag coefficients for both wings at  $0^\circ$ , which is due to a severe underestimation of the profile drag coefficients. The reason for this underestimation is unknown. As expected, the induced drag

coefficients of both the smooth and tubercled wings at  $0^\circ$  are negligible.

From Fig. 9a) and b) tubercles reduce the profile drag coefficient by approximately 20% from  $0^\circ$  to  $6^\circ$  while increasing it by approximately 50% at  $9^\circ$  and  $12^\circ$ . The reason for the sudden increases at  $9^\circ$  and  $12^\circ$  will be elucidated from the spanwise drag coefficient distributions presented in 3.3. From  $0^\circ$  to  $6^\circ$  tubercles do not significantly affect the induced drag coefficient as shown by Figs. 9b) and c). At  $9^\circ$  tubercles reduce the induced drag coefficient by 8% before increasing it by 34% at  $12^\circ$ . Fig. 10 shows the corrected induced, profile, and total drag coefficients of the tubercled wing compared to the smooth wing. The drag coefficients presented in this figure are for when both wings produce the same lift coefficients. As found in the uncorrected case, from  $0^\circ$  to  $6^\circ$ , tubercles reduce the profile drag coefficient by approximately 20%. At  $9^\circ$ , tubercles also increase the profile drag coefficient, however, by a significantly greater amount, 115%, which the authors attribute to greater flow separation over the tubercled wing than the smooth wing. Fig. 10 indicates that if the tubercled wing produces the same lift coefficient as the smooth wing from  $0^\circ$  to  $9^\circ$ , tubercles would have negligible effects on the induced drag coefficient. From  $0^\circ$  to  $6^\circ$ , when the tubercled wing produces the same lift coefficient as the smooth wing, tubercles would still reduce the total drag coefficient. In addition, at  $9^\circ$ , tubercles would still increase the total drag coefficient.

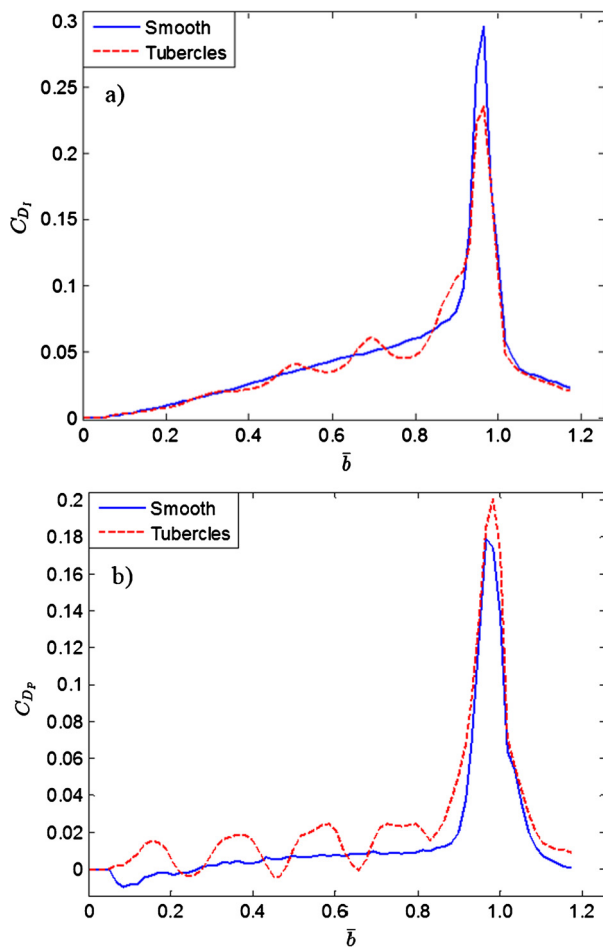


Fig. 13. Spanwise induced, a), and profile, b), drag coefficient distributions for smooth and tubercled wings at  $9^\circ$ .

### 3.3. Spanwise drag coefficient distributions

The first integrands of Eqs. (4) and (8) have been integrated in the wing thickness direction to produce spanwise drag coefficient distributions, which are given in Figs. 11 to 14.

Note that the spanwise drags were non-dimensionalised to the local chord. There was an average spanwise velocity of approximately 0.4 m/s for all wings towards the wingtip, as given by the Cobra probe readings. Therefore, while the wings have a span of 330 mm, the “virtual” wingtip was taken as the position of the peak in the profile drags, which resulted in 348 mm. The local chords were then computed by a simple translation of 348/330 down the wingspan. The spanwise drag coefficient distributions of the wings at  $3^\circ$  have not been included as no new trends appeared. At  $0^\circ$  the induced drag coefficient is negligible, therefore, the spanwise induced drag coefficient distributions are approximately 0. For all non-zero degree angles of attack tubercles modulate the spanwise induced drag coefficient into local minima and maxima.

They become more pronounced towards the wingtip. Similarly, for all angles of attack, tubercles modulate the spanwise profile drag coefficient, however, the modulation is relatively constant along the span. The locations of these local minima and maxima have been determined by tracing through the vorticity distribution in Fig. 15. The local maxima and minima in the spanwise profile drag coefficient tend to occur in regions of common Upwash and downwash, respectively, which correspond to the troughs and

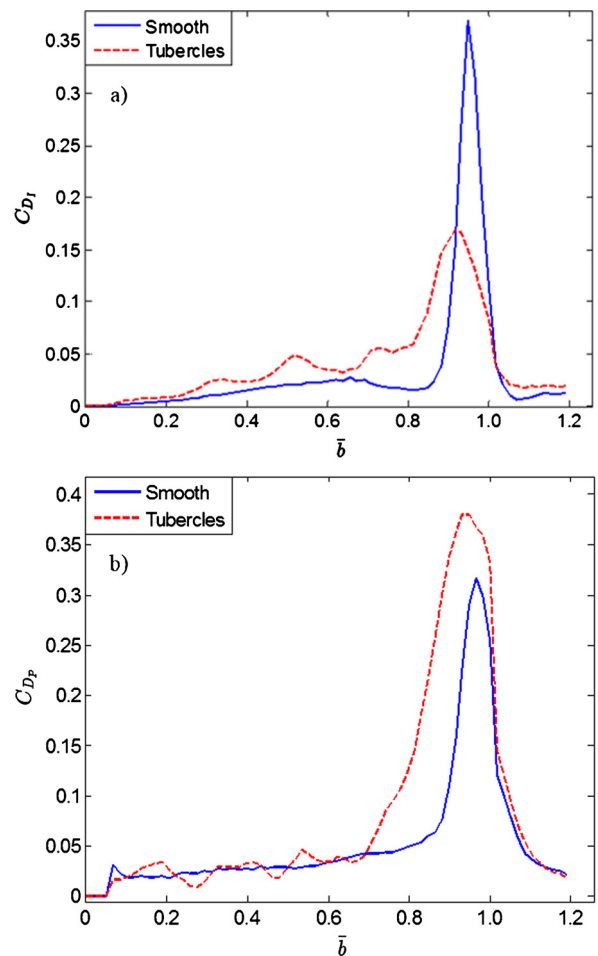


Fig. 14. Spanwise induced, a), and profile, b), drag coefficient distributions for smooth and tubercled wings at  $12^\circ$ .

peaks, respectively. Conversely, the local maxima and minima of the spanwise induced drag coefficient tend to occur in the regions of common downwash and upwash, respectively. At  $0^\circ$  there is a reduction in the profile drag coefficient in the wingtip region, however at  $3^\circ$  and  $6^\circ$  there is little difference in the profile drag coefficient distributions between the wings in the wingtip region, therefore, the reductions in the profile drag coefficient in Fig. 9 must largely result from reductions over the wingspan.

At  $9^\circ$ , while the vorticity contour plots in Fig. 6 do not indicate obvious flow separation in the wingtip region of the tubercled wing, the sudden increase in the tubercled wing’s spanwise profile drag coefficient compared to the smooth wing indicates flow separation in this region. Furthermore, in the wingtip region, the tubercled wing increases the profile drag coefficient, but reduces the induced drag coefficient, therefore, flow separation is likely occurring in this region. This flow separation explains the sudden increase in the profile drag coefficient at  $9^\circ$  as presented in Fig. 9. At  $12^\circ$  the tubercled wing has largely stalled in the wingtip region as the profile drag coefficient has greatly increased and the induced drag coefficient has greatly reduced in Fig. 14. The earlier flow separation on a tubercled wing has also been noted in other works such as Johari et al. [22] and Murray et al. [23]. Interestingly, at  $0^\circ$  and  $3^\circ$  the local maxima in the profile drag coefficient distributions are sharp, however, from  $6^\circ$  onwards, these local maxima become flatter, as labelled on Fig. 12b), suggesting that flow is separating in the troughs.

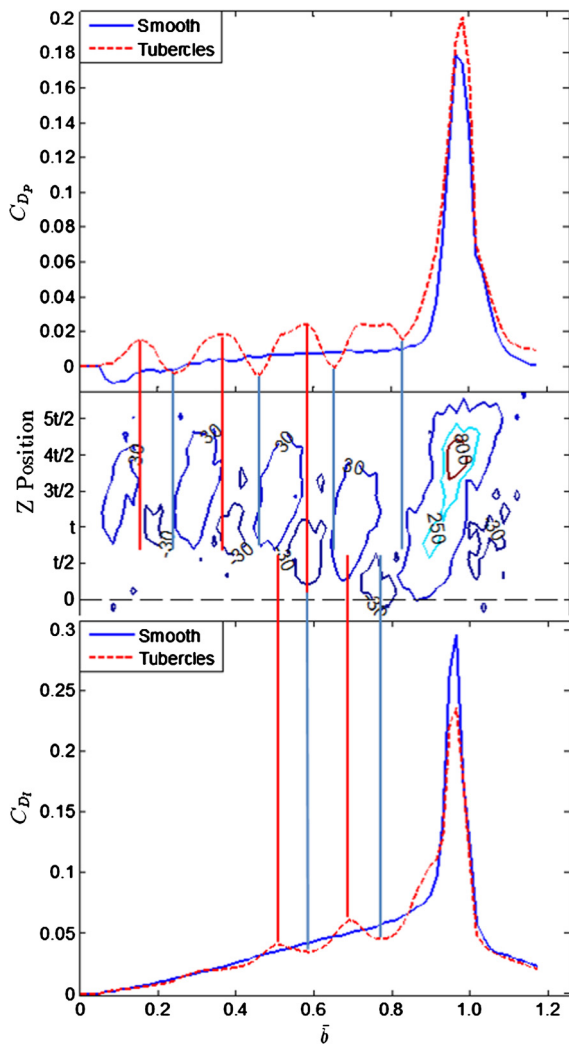


Fig. 15. Locating the local minima and maxima in the induced and profile spanwise drag distributions with the vorticity contour plot;  $9^\circ$ .

### 3.4. Location of drag changes

Fig. 16 shows the relative change in the profile, induced, and total drag coefficients over the wingspan, from 0 to 1, and the wingtip, from 1 onwards. For all angles of attack, the majority of the change in the profile drag coefficient occurs over the wingspan, with the wingtip region only accounting for approximately 20% of the change. For  $0^\circ$ ,  $6^\circ$ ,  $9^\circ$ , and  $12^\circ$  the vast majority of the change in the induced drag occurs over the wingspan, with minimal change occurring in the wingtip region. However, at  $3^\circ$  the converse is true. For all angles of attack, the majority of the change in the total drag coefficient arises from over the wingspan. These trends suggest that to achieve the greatest change in the drag and its components, and hence the greatest potential reductions, tubercles should be implemented along the entire leading edge.

## 4. Conclusion

Wake surveys were conducted at  $0^\circ$ ,  $3^\circ$ ,  $6^\circ$ ,  $9^\circ$ , and  $12^\circ$  on two swept wings, one with a smooth leading edge and one with a tubercled leading edge. Sweeping a tubercled wing resulted in an asymmetry in the strengths of the vortices produced by a single tubercle. Additionally, the strengths of the tubercle vortices increased with angle of attack. Below  $3^\circ$  there was little difference between the strength of the wingtip vortices of either wing, while

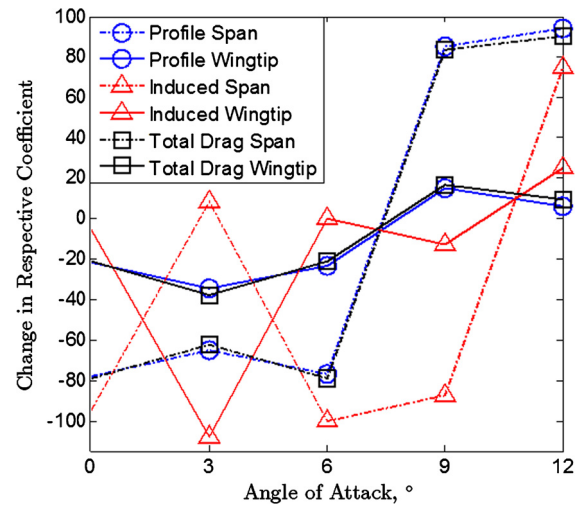


Fig. 16. Relative changes in the profile, induced, and total drag coefficients over span and wingtip. Note: negative percentage means reduction.

above  $6^\circ$  the smooth wing produced a stronger wingtip vortex. For angles of attack  $6^\circ$  and below the tubercled wing reduced the profile drag coefficient, but had little effect on the induced drag coefficient. From  $9^\circ$  onwards the tubercled wing increased the profile drag coefficient and reduced the induced drag coefficient, ostensibly because of flow separation near the wingtip region. Corrected drag coefficients of the tubercled wing when producing the same lift coefficient as the smooth wing were calculated at  $0^\circ$ ,  $3^\circ$ ,  $6^\circ$ , and  $9^\circ$ . The same trends were found as in the uncorrected case, except at  $9^\circ$  where tubercles did not significantly affect the induced drag coefficient.

The smooth wing produced relatively uniform profile and induced drag coefficient distributions along its entire span with peaks at the wingtip. Conversely, tubercles modulated the profile and induced drag coefficients along the entire span, with local maxima and minima in the profile drag coefficients forming in the troughs and over the peaks, respectively. Typically, tubercles produced local maxima and minima in the induced drag coefficients over the peaks and in the troughs, respectively. The majority of change in either the profile or induced drag coefficients occurred over the wingspan, but small changes were also observed in the wingtip region.

### Conflict of interest statement

There is no conflict of interest.

### Acknowledgements

Funding: This work was supported by The Sir Ross and Sir Keith Smith Fund (Smith Fund) ([www.smithfund.org.au](http://www.smithfund.org.au)). The authors thank Eyad Hassan and Peter Lanspeary at The University of Adelaide for their assistance in calculating the vortices' circulations.

### References

- [1] C.M. Jurasz, V.P. Jurasz, Feeding modes of the Humpback Whale, *Megaptera Novaeangliae*, in *Southeast Alaska*, Sci. Rep. Whales Res. Inst. 31 (1979) 69–83.
- [2] F.E. Fish, P.W. Weber, M.M. Murray, L.E. Howle, The tubercles on Humpback Whales' Flippers: application of bio-inspired technology, *Integr. Comp. Biol.* 51 (1) (2011) 203–213.
- [3] H.T. Pedro, M.H. Kobayashi, Numerical study of stall delay on Humpback Whale Flippers, in: *AIAA Aerospace Sciences Meeting and Exhibit*, Reno, 2008.
- [4] M.J. Stanway, Hydrodynamic effects of leading-edge tubercles on control surfaces and in flapping foil propulsion, M.S. Thesis, Massachusetts Institute of

- Technology, MA, February 2008.
- [5] T. Swanson, K.M. Isaac, Biologically inspired wing leading edge for enhanced wind turbine and aircraft performance, in: *AIAA Theoretical Fluid Mechanics Conference*, Honolulu, 2011.
- [6] K.L. Hansen, R.M. Kelso, B.B. Dally, Performance variations of leading-edge tubercles for distinct airfoil profiles, *AIAA J.* 49 (1) (2011) 185–194, <http://dx.doi.org/10.2514/1.j050631>.
- [7] B. Stein, M.M. Murray, Stall mechanism analysis of Humpback Whale Flipper models, in: *Unmanned Untethered Submersible Technology (UUST)*, Autonomous Undersea Systems Inst., Lee, NH, 2005.
- [8] M.D. Bolzon, R.M. Kelso, M. Arjomandi, Tubercles and their applications, *J. Aerosp. Eng.* 29 (1) (2016), [http://dx.doi.org/10.1061/\(ASCE\)AS.1943-5525.11.0000491](http://dx.doi.org/10.1061/(ASCE)AS.1943-5525.11.0000491).
- [9] D.S. Miklosovic, M.M. Murray, L.E. Howle, F.E. Fish, Leading-edge tubercles delay stall on Humpback Whale (*Megaptera Novaeangliae*) flippers, *Phys. Fluids* 16 (5) (2004) L39–L42, <http://dx.doi.org/10.1063/1.1688341>.
- [10] M.D. Bolzon, R.M. Kelso, M.A. Arjomandi, Force measurements and wake surveys of a swept tubercled wing, *J. Aerosp. Eng.* (2016), accepted for publication, [http://dx.doi.org/10.1061/\(ASCE\)AS.1943-5525.0000683](http://dx.doi.org/10.1061/(ASCE)AS.1943-5525.0000683).
- [11] M.D. Bolzon, R.M. Kelso, M. Arjomandi, The effects of tubercles on swept wing performance at low angles of attack, in: *Australasian Fluid Mechanics Conference*, RMIT, Melbourne, 2014.
- [12] TFI, Getting Started Series 100 Cobra Probe, Turbulent Flow Instrumentation Pty. Ltd., 2011.
- [13] I.C. Shepherd, A four hole pressure probe for fluid flow measurements in three dimensions, *J. Fluids Eng.* 103 (1981) 590–594.
- [14] E.R. Hassan, T.C. Lau, R.M. Kelso, Accuracy of circulation estimation schemes applied to discretised velocity field data, in: *Australasian Fluid Mechanics Conference*, Gold Coast, 2007.
- [15] G.W. Brune, Quantitative low-speed wake surveys, *J. Aircr.* 31 (2) (1994) 249–255, <http://dx.doi.org/10.2514/3.46481>.
- [16] K. Kusunose, J.P. Crowder, Extension of wake-survey analysis method to cover compressible flows, *J. Aircr.* 39 (6) (2002) 954–963, <http://dx.doi.org/10.2514/2.3048>.
- [17] R.J. Moffat, Contributions to the theory of single-sample uncertainty analysis, *J. Fluids Eng.* 104 (June 1982) 250–258.
- [18] J.P. Holman, *Experimental Methods for Engineers*, 6th ed., McGraw-Hill, New York, 1994, pp. 48–51.
- [19] R.H. Dieck, *Measurement Uncertainty: Methods and Applications*, The Instrument Society of America, North Carolina, 1992.
- [20] K.L. Hansen, Effect of leading edge tubercles on airfoil performance, Ph.D. Dissertation, The School of Mechanical Engineering, The University of Adelaide, South Australia, 2012.
- [21] J.C. Lin, Review of research on low-profile vortex generators to control boundary-layer separation, *Prog. Aerosp. Sci.* 31 (2002) 389–420, [http://dx.doi.org/10.1016/S0376-0421\(02\)00010-6](http://dx.doi.org/10.1016/S0376-0421(02)00010-6).
- [22] H. Johari, C. Henoch, D. Custodio, A. Levshin, Effects of leading-edge protuberances on airfoil performance, *AIAA J.* 45 (11) (2007) 2634–2642, <http://dx.doi.org/10.2514/1.28497>.
- [23] M.M. Murray, D.S. Miklosovic, F. Fish, L. Howle, Effects of leading edge tubercles on a representative whale flipper model at various sweep angles, in: *Proceedings of Unmanned Untethered Submersible Technology*, UUST, NH, US, 2005.